Acta Materialia 219 (2021) 117257

Contents lists available at ScienceDirect

Acta Materialia

journal homepage: www.elsevier.com/locate/actamat

Rheology of amorphous olivine thin films characterized by nanoindentation

Paul Baral[a,*], Andrey Orekhov[a,b], Ralf Dohmen[c], Michaël Coulombier[a], Jean Pierre Raskin[d], Patrick Cordier[e,f], Hosni Idrissi[a,b], Thomas Pardoen[a]

[a] Institute of Mechanics, Materials and Civil Engineering (IMMC), UCLouvain, B-1348, Louvain-la-Neuve, Belgium
[b] EMAT, University of Antwerp, Groenenborgerlaan 171, B-2020, Antwerp, Belgium
[c] Institute of Geology, Mineralogy, and Geophysics, Ruhr-University Bochum, Universitätsstr. 150, 44801 Bochum, Germany
[d] Institute of Information and Communication Technologies, Electronics and Applied Mathematics (ICTEAM), UCLouvain, B-1348, Louvain-la-Neuve, Belgium
[e] Univ. Lille, CNRS, INRAE, Centrale Lille, UMR 8207-UMET-Unité Matériaux et Transformations, Lille, France
[f] Institut Universitaire de France, Paris, France

ARTICLE INFO

Article history:
Received 15 May 2021
Revised 10 August 2021
Accepted 13 August 2021
Available online 19 August 2021

Keywords:
nanoindentation
rheology
glass
amorphous olivine
relaxation

ABSTRACT

The rheological properties of amorphous olivine thin films deposited by pulsed laser deposition have been studied based on ambient temperature nanoindentation under constant strain-rate as well as relaxation conditions. The amorphous olivine films exhibit a viscoelastic-viscoplastic behavior with a significant rate dependency. The strain-rate sensitivity m is equal to ~ 0.05 which is very high for silicates, indicating a complex out-of-equilibrium structure. The minimum apparent activation volume determined from nanoindentation experiments corresponds to Mg and Fe atomic metallic sites in the $(Mg,Fe)_2SiO_4$ crystalline lattice. The ambient temperature creep behavior of the amorphous olivine films differs very much from the one of single crystal olivine. This behavior directly connects to the recent demonstration of the activation of grain boundary sliding in polycrystalline olivine following grain boundary amorphization under high-stress.

Introduction

Olivine, a silicate with composition $(Mg,Fe)_2SiO_4$, is the major constituent (60 to 80 %) of the Earth's mantle up to *ca.* 410 km deep where it transforms into a high-pressure polymorph, called wadsleyite. The mechanical properties of olivine are of primary importance in geodynamics since this mineral controls the rheology of the upper mantle which ensures the mechanical coupling between the ductile asthenospheric mantle (involved in mantle convection) and the lithospheric plates. Despite years of research, the plasticity of olivine is still insufficiently understood. Investigations in this field have focused mostly on the plasticity mechanisms by dislocation glide (and climb). Only two glide directions are active [100] and [001] in this orthorhombic mineral [1]. The conditions are therefore not met to deform a polycrystalline aggregate homogeneously. The work of Hirth and Kohlstedt [2] suggested that grain boundary sliding may be an important deformation mechanism (see also Hansen et al. [3] and Ohuchi et al. [4]). The active mechanisms responsible for grain boundary sliding are very poorly characterized and understood in olivine. The presence of disclinations has been reported recently in olivine grain boundaries [5]. On the other hand, approaches based on disconnections are currently attracting the attention of the community (*e.g.* Han et al. [6], Hirth et al. [7]) but these defects have not yet been detected in olivine. A recent study [8] has shown that under high stresses, the grain boundaries in olivine are likely to amorphize and that, above the glass transition temperature, this allows a very strong activation of grain boundary sliding [9]. The mechanical properties of amorphous olivine (named hereafter "a-olivine") are not yet documented. It is indeed very difficult to quench this silicate in amorphous form after fusion without implying very fast quenching. Recently, Kranjc et al. reported room temperature amorphization of single crystal olivine, within shear bands, during micro pillar compression creep tests [10]. From a theoretical point of view, Gouriet et al. [11] studied the limits of the mechanical stability of olivine in response to elongation or shear. The authors showed that in forsterite at 0 K, the instability threshold can be as low as 6 GPa when shear is applied along the (100) plane.

* Corresponding author.
E-mail address: paul.baral@uclouvain.be (P. Baral).

https://doi.org/10.1016/j.actamat.2021.117257

In response to this new interest for measuring and understanding the mechanical behavior of a-olivine, a study by nanoindentation of pulse laser deposited (PLD) a-olivine thin films is proposed. The highly out-of-equilibrium conditions of the PLD method is one of the only ways to stabilize an amorphous olivine structure with a controlled stoichiometry. Nanoindentation has become, over the past decades, a versatile nanomechanical testing method allowing extensive measurements not restricted to classical hardness and modulus [12,13]. More specifically, several strain-rate sensitivity measurement methods have been developed to investigate rheological properties of materials from room to high temperatures [14,15]. Even though this technique is widely used for engineering materials such as metals [16], ceramics [17,18], polymers [15,19], in the bulk or in thin film coatings [20,21], the application to the characterization of minerals remains rare [22–26]. The objective of this study is to determine the rheological properties of pulsed laser deposited (PLD) a-olivine films together with the atomistic mechanism responsible for this behavior. The results are discussed to deduce possible implications on Earth's mantle behavior.

Material and methods

Pulsed Laser Deposition of a-olivine

For the preparation of thin films synthetic, polycrystalline pellets of olivine with a nominal composition of $Fe_{0.2}Mg_{1.8}SiO_4$ were ablated using a pulsed laser beam with a frequency of 10 Hz, a wavelength of 192 nm, and at a laser fluence of approximately 5 J/cm^2. Details on the setup can be found in the work of Dohmen et al. [27]. The deposition rates were in the range between 10-20 nm/min. The depositions were performed at a background vacuum pressure of 1×10^{-5} mbar (1×10^{-3} Pa) and at room temperature. At these conditions it has been demonstrated in the past that the silicate film of an olivine-like composition is amorphous and chemically homogeneous [27,28]. The depositions were performed on clean silicon wafers oriented [100]. The resulting surface topography is small with a typical roughness of less than 1 nm [27], as measured by atomic force microscopy (AFM). The PLD set-up does not allow the rotation of the substrate during deposition and the plasma jet coming out of the target is relatively small compared to the substrate. This results in a deposited layer with some variation of the thickness. The thickness has to be measured for every sample in which indentation is performed. Two samples were used in this study with a measured thickness equal to 315 nm and 252 nm, respectively. The first sample was used for the classical constant strain-rate (CSR) indentation tests and the second one for the indentation relaxation experiments.

Nanoindentation data reduction scheme

The hardness is defined as the ratio of the applied force F over contact area A_c under loading.

$$H = \frac{F}{A_c}. \tag{1}$$

A schematic of the tip penetrating into a film with a thickness t_f is shown in Fig. 1.a. The tip used has a Berkovich geometry. For simplification, the Berkovich geometry is approximated by a cone of equivalent contact area as function of indentation depth defined by the half-included angle θ (see Fig. 1.a). The contact depth h_c can be calculated from the penetration depth h using the Oliver and Pharr model [29] to account for the contact geometry – *i.e.* sink-in in this case, see Fig. S1 in Supplementary materials – as:

$$h_c = h - 0.75\frac{F}{S}. \tag{2}$$

The tip contact area function $A_c(h_c)$ is calibrated on fused silica prior the experiments with the polynomial function described with Equ. (23) in reference [30]. The contact area was confirmed from the residual imprints' geometries on a-olivine – *i.e.* absence of pile-up – (See Fig. S1 in Supplementary materials).

The reduced contact modulus is defined by:

$$E_c'^* = \frac{\sqrt{\pi}}{2}\frac{S}{\sqrt{A_c}} \tag{3}$$

with S the contact stiffness [29]. The reduced modulus E'^* is calculated from $\frac{1}{E_c'^*} = \frac{1}{E'^*} + \frac{1-\nu_i^2}{E_i'}$, with the Young's modulus and Poisson ratio of the diamond being, respectively, $E_i' = 1150$ GPa and $\nu_i = 0.1$. The Young's modulus of the material is then determined as $E\prime = E'^*(1-\nu^2)$, where ν is the Poisson ratio.

In the framework of thin film indentation, the effective Young's modulus of the film E_f' must be deconvoluted from the mechanical interactions with the substrate of the apparent Young's modulus E_{app}'. The model of Bec et al. [31] is based on the deformation of a purely elastic bilayer system indented by a flat cylindrical punch. The apparent reduced modulus $E_{app}'^*$ is a combination of the substrate and of the film reduced moduli, $E_s'^*$ and $E_f'^*$, respectively, writing

$$E_{app}'^* = \frac{1 + 2t/\pi a_c}{2}\left(\frac{\pi a_c E_f'^* E_s'^*}{2E_s'^* t + \pi a_c E_f'^*}\right), \tag{4}$$

with $t = t_f - h_c/3$ the equivalent film thickness and $a_c = \sqrt{A_c/\pi}$ the equivalent contact radius. Bec's model is an approximation based on flat cylindrical punch indentation where $t = t_f$. The approximation is relatively correct for a Berkovich tip which has a large open angle. Nevertheless, a further correction proposed by Bec et al. can be used to account for the reduction of effective film thickness when indenting with a pyramidal tip. This correction is based on the volume reduction due to the deformed material under the tip. If the volume occupied by the tip is subtracted, the equivalent thickness of the film deformed by a flat cylindrical punch of radius a_c becomes $t = t_f - h_c/3$ [31]. The reduced modulus $E_f'^*$ is a fitting parameter in Equ. (4).

In a nanoindentation relaxation test, the loading is composed of three steps: (1) a constant strain-rate (CSR) loading up to a prescribed contact stiffness, (2) a hold segment during which contact stiffness is maintained constant while the load is monitored and (3) a constant unloading rate. The hardness H is calculated, during the relaxation step, by the following relationship:

$$H = \frac{F}{A_c} = \frac{4F}{\pi}\left(\frac{E_c'^*}{S}\right)^2. \tag{5}$$

When using Equ. (5), it is assumed that $E_c'^*$ is independent of time, so that the contact area remains constant. The value of the reduced contact modulus is calculated from the end of the loading segment, with the Continuous Stiffness Measurement module (CSM®). This CSM® module allows the measurement of the stiffness continuously along the loading steps by applying a displacement oscillation of small amplitude and frequency ω in addition to the quasi-static loading – this creates micro-unloading segments along the entire indentation loading. An asynchronous detector is used to extract the stiffness from the load over displacement response to the dynamic solicitation.

In order to extract the rheological properties of the material, the evolution of hardness must be compared to the strain-rate. However, during a relaxation step, the tip is motionless [15,32] which makes impossible the use of the classically defined indentation strain-rate – *i.e.* $\dot{\epsilon}_{ind} = \dot{h}/h$, where $\dot{h}$ is the displacement rate. Therefore, the expression of the strain-rate is derived from imposing the total strain-rate to be equal to $\dot{\epsilon} = 0$, $\dot{\epsilon} = \dot{\epsilon}^{el} + \dot{\epsilon}^{vpl} = 0$

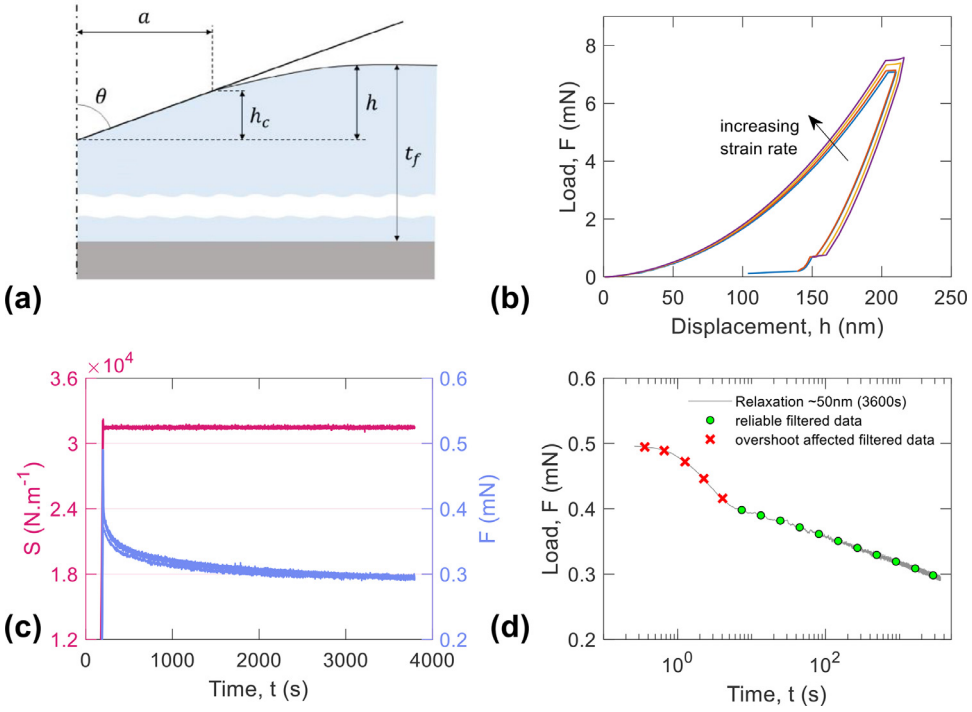

Fig. 1. Overview of the different indentation methods: (a) schematics of the indenter and sample geometry, with the main parameters used in the data reduction scheme; (b) load-penetration curves for six different indentation strain-rates applied to a-olivine, with higher loads reach at a given depth when increasing indentation strain-rate; (c) contact stiffness and load as a function of time during 50 nm relaxation experiments. Six experiments are displayed; and (d) raw load data as a function of time during the relaxation step and example of post-treatment.

[15]. By considering a time-independent Young's modulus – *i.e.* neglecting viscoelasticity –, the relaxation strain-rate can thus be expressed as:

$$|\dot{\epsilon}_r| = \frac{|\dot{\sigma}_r|}{E'_{app}}, \tag{6}$$

where E'_{app} is the Young's modulus of the composite film/substrate materials – *i.e.* without correction from substrate effect – and σ_r is the representative stress which is proportional to hardness, in the form:

$$\sigma_r = \frac{H}{c}, \tag{7}$$

where c is the reduced contact pressure which depends on the indenter geometry and the $H/E\prime$ ratio. The reduced contact pressure of a rigid plastic material is given by Tabor [16] – *i.e.* $\frac{H}{E\prime} \approx 0$ and $c = 3$ – which is well suited for metals. This factor tends to decrease with increasing H/E ratio, when the material response to indentation is no more predominantly plastic – for instance in fused silica with $\frac{H}{E\prime} = 0.125$ and c is equal to 1.5 [33]. Kermouche et al. give an expression of the factor c [34,35] which is calculated in the framework of elastoplastic materials. This factor is needed to extract the representative stress in this study, see further calculation in reference [15]. The reduced contact pressure c ranges between 2.37 and 2.42 depending on the indentation depth to film thickness ratio. The representative stress is post-treated to decrease the noise to signal ratio prior numerical differentiation. This treatment involves the re-sampling of the force signal over a time-scale of 0.6 (in log-time scale), see Fig. 1.d.

The strain-rate sensitivity m characterizes the variation of yield stress σ_y as a function of the applied strain-rate. In the context of power law creeping materials, a constant value of m is assumed when a single creep mechanism dominates, with

$$\sigma_y = B\ \dot{\epsilon}^m, \tag{8}$$

where B is the strength coefficient. In indentation, the rate sensitivity can be related to the variation of hardness with indentation strain-rate [36,37]. As proposed by Kermouche et al. and Elmustafa et al. [36,38,39] the variation of representative stress σ_r with the indentation strain-rate, is used:

$$m = \frac{\mathrm{d}\ln(\sigma_r)}{\mathrm{d}\ln(\dot{\epsilon})}, \tag{9}$$

with strain-rate $\dot{\epsilon}$ being either the indentation strain-rate $\dot{\epsilon}_{ind}$, in the case of constant strain-rate tests, or $\dot{\epsilon}_r$ in the case of relaxation experiments.

The apparent activation volume V^* is an atomistic characteristic of the fundamental deformation mechanism related to the elementary material volume undergoing the plastic event. It is proportional to the inverse of the strain-rate sensitivity as $V^* = \alpha kT/m\sigma_r$, with k the Boltzmann constant and T the absolute temperature [40,41]. It can thus be determined as

$$V^* = \alpha kT\left(\frac{\mathrm{d}\ln(\dot{\epsilon})}{\mathrm{d}\sigma_r}\right), \tag{10}$$

in which the stress and strain-rate are replaced by the representative stress σ_r and strain-rate $\dot{\epsilon}$. The α parameter is a constant that depends on the link between the shear stress needed to activate the plastic event and the representative stress value. In the following developments $\alpha = \sqrt{3}$ [42,43]. Hence, the extraction of the rate sensitivity indicator is a powerful way to reveal information on the atomistic mechanisms controlling the deformation process.

Nanoindentation test methods

Indentation experiments have been performed using a Nanoindenter G200® (KLA Tencor) with a Dynamic Contact Module (DCM V2®) head providing very accurate measurements at low loads and displacements. The maximum force of the device is equal to 45 mN with a resolution of 1 nN. The displacement is measured with a

Table 1
Long-term relaxation tests' parameters. With S_{hold} the stiffness maintained constant during the relaxation segment and h_{equiv} the corresponding penetration depth.

Tests	Hold duration (min)	S_{hold} (N.m^{-1})	h_{equiv} (nm)	CSM amplitude (nm)
1	10	1.58×10^4	20	1
2	60	3.8×10^4	50	2
3	60	6.1×10^4	70	2

resolution of 0.2 pm. A diamond Berkovich tip with a very low tip defect height [32,44] ($h_d \approx 3\ nm$) was used. Coated silicon wafers were glued to the sample holders using a thermoplastic glue (heating during 1 min at 150°C) and a cyano-acrylate glue (at room temperature). This ensures that PLD a-olivine is not subjected to crystallization in this temperature range. No differences were detected between the two sets of samples.

Two types of tests have been carried out: classical constant strain-rate indentation (CSR) [45] (see Fig. 1.b) and indentation long-term relaxation tests [15,32] (see Fig. 1.c). This last method has only been very recently developed. The CSR tests were performed at different prescribed strain-rates equal to $\frac{\dot{F}}{F}$ =0.05, 0.1, 0.3 and 0.5 s^{-1} resulting in representative indentation strain-rates quantified by $\frac{\dot{h}}{h}$ = 0.03, 0.06, 0.18 and 0.3 s^{-1} up to a maximum depth of 200 nm as shown in Fig. 1.b, in which one representative experiment from each loading rate is displayed. Here again, $\dot{F}$ and $\dot{h}$ stand for the load and displacement rates, respectively. The load increases at equivalent penetration depth when increasing the indentation strain-rate. The continuous stiffness measurement (CSM) was set up at a frequency of 75 Hz with an amplitude of 1 nm. For each loading conditions six experiments were performed. The long-term relaxations were performed at three different indentation depths in order to account for a possible substrate effect – and as well, confinement level of the film – on the strain-rate sensitivity measurements. Indentation strain-rates before the hold segment was set to $\frac{\dot{h}}{h}$ = 0.06 s^{-1}. The indentation parameters used for these tests are displayed in Table 1. The contact stiffness was maintained constant with a proportional-integral loop. The gains were adjusted to minimize the overshoot and the time response to reach the target value [15]. For all relaxation tests, the maximum overshoot did not exceed 3.1 % of the target contact stiffness. The peak to peak amplitude of the stiffness measurement were evaluated at 500, 700 and 1000 N.m^{-1} for the experiments performed at 20, 50 and 70 nm equivalent penetration depth, respectively. These represent less than 3 % of the target contact stiffness. The time necessary for the contact stiffness to stabilize after the overshoot was 10 seconds for the 50 and 70 nm experiments and 4 seconds for the 20 nm ones. Hence, relaxation measurements were considered valid only after these periods of time. Fig. 1.c displays the variation of the contact stiffness and of the load during the relaxation step, as a function of time. Six experiments performed at 50 nm are displayed. The very good control of the contact stiffness over one-hour experiment can be appreciated as well as the reproducibility of the load response even for long step durations. Fig. 1.d represents an example of data post treatment on the load signal, as explained in the former section. The red crosses stand for the overshoot-affected data, which are not used for the determination of the mechanical properties, and the green circles correspond to representative data.

TEM characterization

Electron transparent thin foils were prepared using a dual-beam focused ion beam (FIB) instrument FEI Helios Nanolab 650. A Pt protection layer was deposited in two steps – by an electron beam, then by an ion beam – in order to avoid FIB damage at the sample surface. The FIB foils were thinned to a thickness < 50 nm. An ion beam of 2 kV/0.2 nA was employed to achieve the final thinning of the specimen and to minimize irradiation damage generated during high-voltage FIB thinning.

Microstructure of a-olivine samples was analyzed by transmission electron microscopy (TEM) using a FEI Osiris microscope operated at 200 kV, and equipped with a XFEG electron source and a high efficiency Super-X system that allows the acquisition of high resolution EDX maps at low dose with a short exposure time. The studies carried out in this work include selected area electron diffraction (SAED), high resolution transmission electron microscopy (HRTEM) and energy dispersive X-ray spectroscopy (EDXS).

Results

Hardness and elastic modulus

The silicon substrate is characterized by a Young's modulus E'_s = 180 GPa, a Poisson ratio ν_s = 0.25 and a reduced modulus E'^*_s = 192 GPa [31]). The reduced modulus of a-olivine deposited on Si is determined following the substrate correction model proposed by Bec et al. (Equ. (4)) with a film thickness t_f of 315 nm.

Each variation of apparent reduced modulus as a function of indentation depth – or contact radius a_c in this case (Equ. (4)) – is fitted for penetration depth ranging from 30 to 80 nm, see Fig. 2.a. This limited range has been selected for two reasons: (i) the lower limit relies on the minimum depth at which the measurement is not affected by surface roughness or tip defect; (ii) the upper limit depends on the transition between two contact regimes. Indeed, as confirmed by SEM observations together with AFM measurements, the contact geometry evolves from sink-in at shallow depths – *i.e.* lower than 70 nm – to pile-up for penetration depths exceeding 100 nm (as a result of significant substrate effect). As the model used to calculate the contact area supposes a sink-in geometry [29], the calculated modulus and hardness will be overestimated in the presence of pile-up. This feature can be observed on Fig. 2.a, where the measured apparent modulus significantly deviates from Bec's model when the contact depth is larger than 70 nm. Thus, the limit of 80 nm for penetration depth – *i.e.* contact depth, h_c = 65 nm – has been chosen to avoid this source of error.

The reduced modulus of a-olivine as a function of indentation strain-rate is shown in Fig. 2.b. The reduced modulus slightly increases with indentation strain-rate, suggesting that a-olivine presents some degree of viscoelasticity. This behavior is not expected since the material is excited with a unique frequency through the CSM® module ($\omega = 75$ Hz). However, the slight variation of reduced modulus with applied strain-rate may arise from a coupled response between the local dynamic solicitation and global applied strain-rate. The film reduced modulus ranges between 103 and 107 GPa, as shown in Fig. 2.b. The Poisson ratio of a-olivine has been estimated from tensile experiments with the Push to Pull set-up in a Transmission Electron Microscope (TEM) (unpublished results). Longitudinal and transverse strains were measured by contrast analysis of bright field images, while the sample was deformed under uniaxial tension. A Poisson ra-

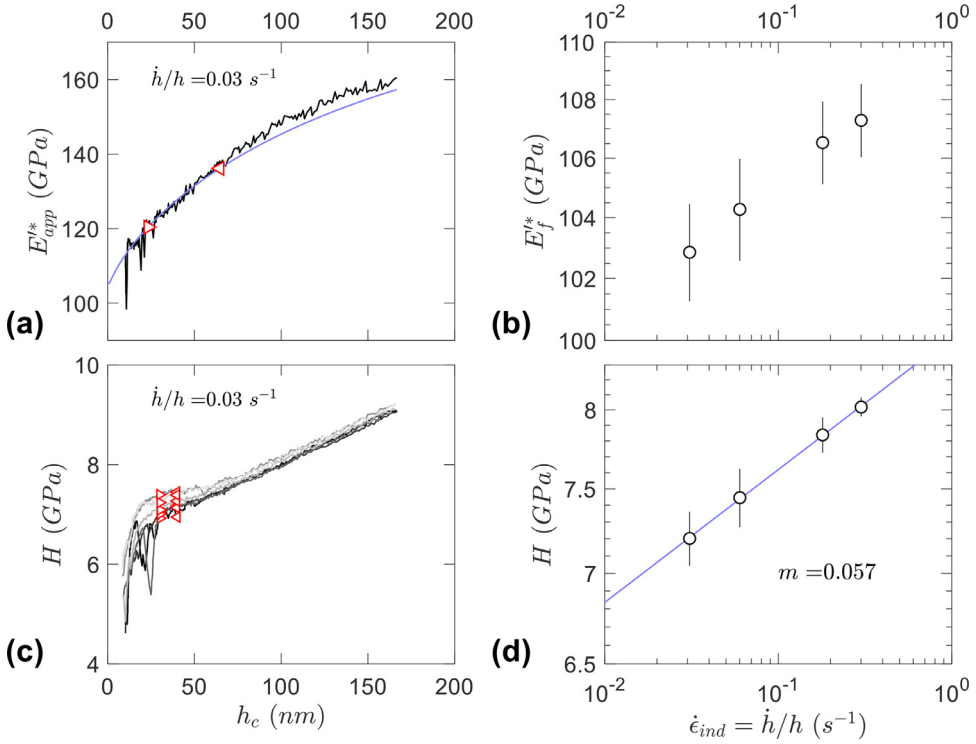

Fig. 2. Variation of reduced modulus and hardness as a function of indentation strain-rate: (a) Measured apparent reduced modulus as a function of contact depth with Equ. (4) fitted between the triangle markers; (b) Variation of the a-olivine reduced modulus as a function of contact depth. Error bars represent the standard deviation calculated on 6 experiments; (c) Variation of hardness as a function of contact depth for a set of six experiments. Triangle markers correspond to the bounds used to determine the average hardness of a-olivine; (d) Hardness as a function of indentation strain-rate. Error bars represent the standard deviation calculated on 6 experiments.

tio of 0.37 was determined. Therefore, the Young's modulus of a-olivine, is found to range between 89 and 92 GPa.

Fig. 2.c displays the variation of hardness with contact depth for a set of six indentations performed at an indentation strain-rate $\frac{\dot{h}}{h} = 0.03\ s^{-1}$. A clear influence of the substrate is observed from 50 nm, as expected. The hardness is measured between h_c = 30 and 40 nm which corresponds to 9.5 % and 12.7 % of the film thickness, respectively, in order to minimize the substrate effect [46]. Triangle markers indicate the bounds between which the average values are calculated (see Fig. 2.c).

The hardness increases from 7 to 8 GPa with indentation strain-rate (see Fig. 2.d), which indicates a significant strain-rate sensitivity as addressed in details in the next section.

A comparison of the apparent reduced modulus E'^{*}_{c} and hardness evolutions as a function of contact depth to the indentation relaxation experiments is performed in Supplementary materials (see Fig. S2) to highlight the small differences in measured values due to substrate effect.

Micro and nano-indentation experiments have been recently reported on single-crystal and polycrystalline olivine [23,24,26]. They highlight a strong size effect – i.e. an increase of hardness at shallow penetration depth – together with a grain size dependency of hardness. These results mitigate the former discrepancies between indentation data on olivine by taking the measurement's length-scale into account. Considering the low thickness of our a-olivine samples, no conclusion about size effect can be drawn. However, the hardness and Young's modulus of a-olivine (between h_c = 30 and 40 nm) can be compared to the literature data on single-crystal olivine. Hardness of a-olivine is 50 % smaller than for single-crystal olivine indented at 76 nm (data from Kumamoto et al. [24]) and 8 % smaller than for single-crystal olivine indented at 7 µm (data adapted from Vickers hardness, Koizumi et al. [26]). The Young's modulus is reported for single crystal olivine to be on the order of 200 GPa [47]. The Young's modulus measured for a-olivine is 55 % smaller than its crystalline counterpart.

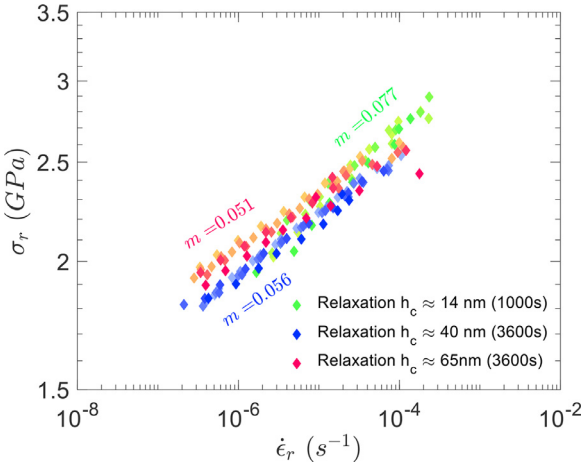

Fig. 3. Variation of the representative stress as a function of strain-rate during relaxation tests. Three sets of six tests are represented with a shaded color corresponding to the approximated indentation depth during relaxation. The average strain-rate sensitivity (Equ. (9)) – or slope of the data in the log-log graph – is displayed for each set of experiment.

Strain-rate sensitivity and activation volume

Fig. 3 displays the representative stress as a function of strain-rate in log-log scale for indentation relaxation tests, measured at different penetration depths. For each depth, six experiments are shown. The results are remarkably reproducible considering the extremely shallow indentation depths and the long relaxation times. The average strain-rate sensitivity m, fitted over the entire set of

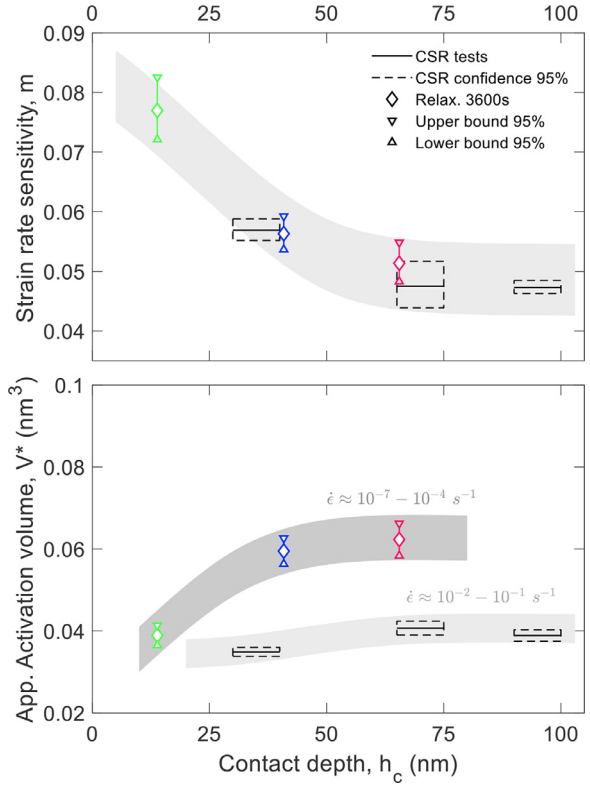

Fig. 4. Variation, as a function of contact depth of: (a) the strain-rate sensitivity and (b) the apparent activation volume. The shaded areas highlight the general trend of the experimental data.

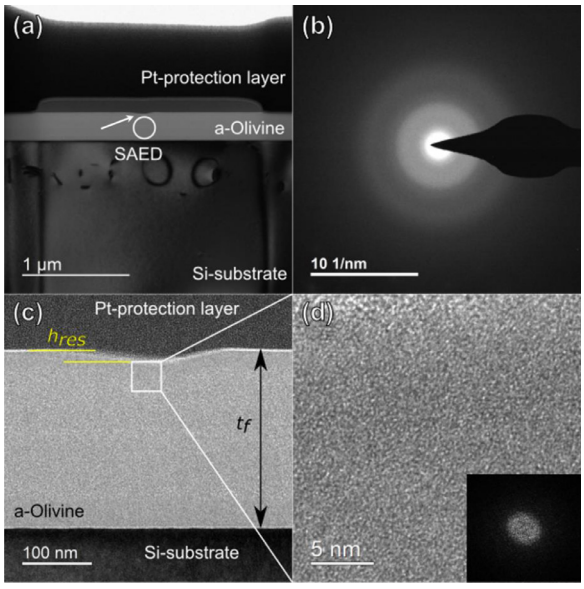

Fig. 5. TEM analysis of a cross sectional FIB foil prepared under an indent from a CSR experiment at 50 nm maximum penetration depth. (a) An overview TEM image of the a-olivine film on the silicon substrate, the white arrow indicates the position of the nanoindentation imprint; (b) Selected area electron diffraction pattern taken from the area delimited by the white circle in (a); (c) Magnified TEM image of the film under the indent tip; (d) HRTEM image of the film exactly under the indent and FFT image confirming the amorphous character of the film after nanoindentation.

experiments with Equ. (9), is displayed together with the curves in Fig. 3. The strain-rate sensitivity of a-olivine varies with indentation depth. This will be discussed in more details in the next sections. Note that the hypothesis of time-independent Young's modulus necessary to calculate the representative strain-rate (see Equ. (6)) is a reasonable assumption considering the low degree of viscoelasticity within this time-scale.

Fig. 4.a shows the variation of m (Equ. (9)) with contact depth. Open symbols correspond to relaxation experiments, with up and down pointing triangles being the 95 % confidence bounds of Equ. (8) fitted over the full set of measurements. Black lines represent the results extracted from CSR experiments and the surrounding dashed boxes are the 95 % confidence bounds of the mathematical fit. The strain-rate sensitivity is constant for contact depth between 20 and 50 % of the film thickness, but increases significantly at shallower depths – *i.e.* +60 % at 20 nm and +20 % at 35 nm.

The apparent activation volume (Equ. (10)) displayed on Fig. 4.b is proportional to the inverse of the strain-rate sensitivity and thus decreases at shallow depth. The apparent activation volume ranges from 0.035 to 0.041 nm^3 for CSR tests and ranges from 0.060 to 0.062 nm^3 for relaxation tests, at moderate indentation depth. The apparent activation volume drops to 0.039 nm^3 at contact depths bellow 25 nm, for the relaxation tests.

TEM characterization of the a-olivine films

The microstructure of a-olivine film under the indent region (indentation imprint of a constant strain-rate (CSR) test performed at 50 nm maximum penetration) was characterized by TEM. The overview TEM image of thin lamella is shown in Fig. 5.a. The film exhibits a fully amorphous structure as can be seen in the SAED pattern of Fig. 5.b, taken from the area delimited by a white circle under the indent in Fig. 5.a. The indent region can be seen in the magnified TEM image in Fig. 5.c where the indent depth value (h_{res}) is equal to 14.8±0.5 nm. The residual depth is equal to the depth measured by AFM (15 and 10 nm, respectively for the CSR and relaxation test, see Fig. S1 in Supplementary materials). The thickness of the film is equal to 252±0.5 nm. In Fig. 5.d, HRTEM image of the olivine film acquired under the indent area shows a fully amorphous structure which is confirmed by the Fast Fourier Transform shown in the inset of the same Fig.. Low- and high- magnification TEM images show no evidences of shear bands under the indent. This observation is also true for the one-hour relaxation experiment. It is in line with the load-displacement data where no pop-in nor burst can be detected.

Discussion

Samples of a-olivine are not available in a bulk form since quenching from the melt requires extreme cooling rates [48]. The only occurrences of a-olivine are found under high stress, either under pressure [11,49], or under high shear stress, within a micro pillar compressed at room temperature [10] and at grain boundaries under high stress conditions [8]. In all cases and particularly at grain boundaries, the thickness of this amorphous phase does not exceed a few nanometers and is therefore extremely confined.

On the strain-rate sensitivity's size effect

At very shallow depths – *i.e.* 20 to 50 nm – the a-olivine rheological behavior differs from larger depths, where it tends to stabilize to a response that is independent of the depth (see Fig. 4.a).

The change of regime at shallow depth is not related to an extrinsic substrate effect. Indeed, measurements of strain-rate sensitivity from CSR tests were performed on a sample with a film thickness of 315 nm and relaxation tests on a sample with a film thickness of 252 nm. The results for strain-rate sensitivity compared well when expressed as a function of the indentation depth

and would have been significantly shifted if they were plotted against h_c/t_f (see Fig. 4.a). This evolution can have several origins, such as an intrinsic material length-scale, a surface effect or a change in contact geometry at shallow depth due to some tip defects. More investigations will be needed to determine the origin of this behavior at shallow depth.

The discussion is now focused on the second regime where the rheological behavior exhibits a plateau – *i.e.* between 50 and 100 nm. The confinement of the film between two harder materials – *i.e.* the diamond tip and the Si substrate – can be, in a first approximation, considered as a proxy of the configuration recently observed of a-olivine films present at the grain boundaries. The strain-rate sensitivity from slightly to moderately confined indentation conditions – *i.e.* h_c/t_f from 0.2 to 0.5 – is equal to 0.049. This value is considered to be representative of a-olivine's creep behavior.

Discussion about atomistic mechanisms

The strain-rate sensitivity is a meaningful indicator of the creep mechanisms active in the material. The high value of m found from this study ($m \approx 0.05$) is first compared to the extensive data set available in the literature for silicate-based glasses. Limbach et al. reported values ranging from 0.015 to 0.028 for alkali borosilicates and 0.0164 for anhydrous soda lime silicates [37]. The strain-rate sensitivity of fused silica has been reported between 0.022 [50] and 0.029 [15] . The strain-rate sensitivity calculated by Limbach et al. is different from the one presented here. They calculated an indentation strain-rate sensitivity based on the evolution of hardness instead of a representative stress, as discussed in the former section. In order to compare the results, it is proposed to use the Fig. 9 in the reference from Elmustafa et al. [36], were the ratio of indentation SRS m_i to uniaxial SRS m is represented against the H/E ratio. The adapted values from Limbach et al. range then from 0.02 to 0.035 for the borosilicates and is 0.02 for the soda lime silicate. The SRS of a-olivine is still nearly two times higher than these references results.

Limbach et al. linked several properties of glasses with the strain-rate sensitivity as related to three types of material arrangements: (1) a high network dimensionality and low packing density; (2) a complex low-dimensional structure; and (3) an arrangement dominated by high packing density [37]. They emphasize that, within the intermediate network dimensionality (2), the strain-rate sensitivity is highly dependent on the chemical and structural properties of the glass and therefore could display large variations of strain-rate sensitivity from one glass to another [37]. Such complex low-dimensional structure is also associated with a Poisson ratio in the range of 0.29 to 0.38 (see Fig. 6 in [37]), which is in line with our estimation from tensile experiment – $\nu = 0.37$. The a-olivine structure should thus be characterized by an intermediate network dimensionality.

The minimum apparent activation volume calculated from nanoindentation is equal to 0.035 nm^3. In amorphous systems, the apparent activation volume V^* is always lower than the physical activation volume Ω_f, with $V^* = \Omega_f.\gamma$ where γ is the transformation strain associated to the local atomistic shuffling mechanism [18,51]. The value of γ for amorphous systems ranges from 0.05 to 0.15, see Argon [51]. If we consider the transformation strain to be $\gamma = 0.1$, the physical activation volume can be compared to the size of atomic sites within the $(Mg,Fe)_2SiO_4$ structure. Birle et al. measured the atomic parameters of forsterite $(Mg_{0.9},Fe_{0.1})SiO_4$ by 3D least-squares X-ray diffraction analysis [52]. The interatomic distance between the surrounding oxygen atoms and the two metal sites M(1) and M(2) occupied by Mg or Fe are 2.103 and 2.135 Å, respectively. If we consider the shape of the sites to be a sphere, the volume of each site would be 0.039 and 0.041 nm^3. These atomic parameters correspond to crystalline olivine and are not to be considered as fully representative of the disordered arrangement in a-olivine which involves some amount of free volume. Nevertheless, it is interesting to note that the activation volume extracted from the apparent value measured by nanoindentation ($\Omega_f \approx 10.V^*$) corresponds to the size of ten to twenty sites of Mg and Fe atoms in crystalline olivine. This would potentially imply that the elementary volume where plastic deformation events take place involves the motion of Mg (or Fe) atoms within the silicate network. According to our measurements, as the SRS m is constant over several orders of magnitude in strain-rate, the corresponding apparent activation volume increases with decreasing strain-rate. Therefore, the number of atoms involved in the viscoplastic deformation events slightly increases at low strain-rates.

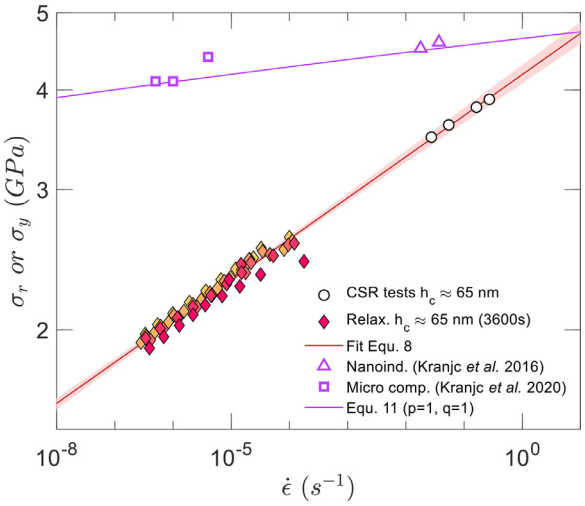

Fig. 6. Representative and yield stress as a function of strain-rate. Comparison between the present nanoindentation study on a-olivine and micromechanical experiments on single crystal olivine [10,23]. The red shaded area around the fitting line highlights the functional 95 % confidence bounds. The error bars on the representative stress and the strain rate for the CSR data are smaller than markers' size.

Implications of the high strain-rate sensitivity of a-olivine

Fig. 6 displays the strain-rate sensitivity of a-olivine compared to single crystal olivine from indentation experiments. For a-olivine, the red plain line represents Equ. (8) fitted to both the CSR and relaxation experiments, with $B = 4.18$ and $m = 0.052 \pm 0.002$. The CSR and relaxation results are perfectly aligned, highlighting a unique creep deformation mechanism over seven orders of magnitude in strain-rate. The high strain-rate sensitivity of a-olivine contrasts with the low temperature rheology of single crystal olivine. We have plotted in Fig. 6 the strain-rate sensitivity of single crystal olivine measured from micro compression creep [10] and nanoindentation [23] experiments by Kranjc et al.. The difference in strain rate sensitivity between olivine and a-olivine is striking. We have fitted the data of Kranjc et al. with a constitutive expression commonly used to describe low-temperature plasticity of olivine, as proposed by Kranjc et al. [23,53].

$$\dot{\epsilon} = A\sigma^2 \exp\left\{-\left(\frac{H_0^*}{RT}\right)\left(1-\left(\frac{\sigma}{\sigma_p}\right)^p\right)^q\right\} \tag{11}$$

with $A = 2.37 \times 10^5$, $H_0^* = 320$ $kJ.mol^{-1}$, $\sigma_p = 5.32$ GPa, $p = 1$ and $q = 1$ [23]. The calculated strain-rate sensitivity m of olivine with this data set revolves around 0.009. Therefore, the strain-rate sensitivity of olivine is approximately five times lower than the one

of a-olivine. This result implies that the strength of a-olivine decreases faster than crystalline olivine when reducing the applied strain rate. This trend is of primary importance from the geophysical point of view since the deformation of the Earth's upper mantle occurs at very low strain rates (down to 10^{-16} -10^{-12} s^{-1}).

However, the temperature involved in the present study is not representative of the Earth' upper mantle conditions, the present results stand thus as an upper bound of a-olivine strength as a function of strain rate. The rheological property of a glass being thermally activated, the strain rate sensitivity can only increase with temperature, until the material exhibits Newtonian flow – i.e. $m = 1$ – close to its glass transition temperature. If this behavior was to be confirmed by further studies at high temperatures, it would imply that the grain boundary sliding observed by Samae et al. [8] in laboratory experiments could play an even more important role in the Earth's upper mantle, at low strain rates.

Conclusion

An extensive nanoindentation study of PLD deposited a-olivine has been performed. Young's modulus, hardness and creep response of this material have been measured and discussed. The indentation relaxation method has been adapted successfully to study thin amorphous film's viscoplastic behavior.

The main findings of this research are the following:

- The a-olivine thin film presents some degree of viscoelasticity with the Young's modulus slightly varying from 89 to 92 GPa with increasing the strain-rate by one order of magnitude.
- TEM observations performed under the indented regions show a strong elastic recovery and no sign of shear bands.
- The a-olivine's hardness is significantly strain-rate sensitive with a strain-rate sensitivity exponent m constant over seven orders of magnitude in strain-rate and equal to 0.052±0.002.
- The high strain-rate sensitivity of a-olivine at ambient temperature contrasts with the much smaller rate sensitivity of single crystal olivine. This result confirms the importance of the applied strain rate on the mechanical behavior of the glassy corresponding material.

These results pave the way to probe the rheological properties' relation to temperature of a-olivine, up to its glass transition temperature. This would allow a better comparison with its natural occurrences and its impact toward Earth's mantle rheology through the activation of grain boundary sliding [8,54].

Declaration of Competing Interest

The authors declare that they have no known competing financial interests or personal relationships that could have appeared to influence the work reported in this paper.

Acknowledgements

This work was supported by the Fonds de la Recherche Scientifique - FNRS under Grant T.0178.19. This project has also received funding from the European Research Council (ERC) under the European Union's Horizon 2020 research and innovation programme under grant agreement No 787198 – TimeMan. H. Idrissi is mandated by the Belgian National Fund for Scientific Research (FSR-FNRS). This work was supported by the FNRS under Grant CDR – J.0113.20. Finally, the authors acknowledge the financial support from the 2020 Marcel de Merre prize awarded by the Fondation Louvain to P. Baral.

Supplementary materials

Supplementary material associated with this article can be found, in the online version, at doi:10.1016/j.actamat.2021.117257.

References

[1] C.B. Raleigh, Mechanisms of plastic deformation of olivine, J. Geophys. Res. 73 (1968) 5391–5406, doi:10.1029/JB073i016p05391.
[2] G. Hirth, D.L. Kohlstedt, Experimental constraints on the dynamics of the partially molten upper mantle: 2. Deformation in the dislocation creep regime, J. Geophys. Res. Solid Earth. 100 (1995) 15441–15449, doi:10.1029/95JB01292.
[3] L.N. Hansen, M.E. Zimmerman, D.L. Kohlstedt, Grain boundary sliding in San Carlos olivine: Flow law parameters and crystallographic-preferred orientation, J. Geophys. Res. 116 (2011) B08201, doi:10.1029/2011JB008220.
[4] T. Ohuchi, T. Kawazoe, Y. Higo, K.I. Funakoshi, A. Suzuki, T. Kikegawa, T. Irifune, Dislocation-accommodated grain boundary sliding as the major deformation mechanism of olivine in the Earth's upper mantle, Sci. Adv. 1 (2015) 1–10, doi:10.1126/sciadv.1500360.
[5] P. Cordier, S. Demouchy, B. Beausir, V. Taupin, F. Barou, C. Fressengeas, Disclinations provide the missing mechanism for deforming olivine-rich rocks in the mantle, Nature 507 (2014) 51–56, doi:10.1038/nature13043.
[6] J. Han, S.L. Thomas, D.J. Srolovitz, Grain-boundary kinetics: A unified approach, Prog. Mater. Sci. 98 (2018) 386–476, doi:10.1016/j.pmatsci.2018.05.004.
[7] J.P. Hirth, G. Hirth, J. Wang, Disclinations and disconnections in minerals and metals, Proc. Natl. Acad. Sci. 117 (2020) 196–204, doi:10.1073/pnas.1915140117.
[8] V. Samae, P. Cordier, S. Demouchy, C. Bollinger, J. Gasc, S. Koizumi, A. Mussi, D. Schryvers, H. Idrissi, Stress-induced amorphization triggers deformation in the lithospheric mantle, Nature 591 (2021) 82–86, doi:10.1038/s41586-021-03238-3.
[9] J. Gasc, S. Demouchy, F. Barou, S. Koizumi, P. Cordier, Creep mechanisms in the lithospheric mantle inferred from deformation of iron-free forsterite aggregates at 900–1200°C, Tectonophysics 761 (2019) 16–30, doi:10.1016/j.tecto.2019.04.009.
[10] K. Kranjc, A.S. Thind, A.Y. Borisevich, R. Mishra, K.M. Flores, P. Skemer, Amorphization and Plasticity of Olivine During Low-Temperature Micropillar Deformation Experiments, J. Geophys. Res. Solid Earth. 125 (2020) 0–3, doi:10.1029/2019JB019242.
[11] K. Gouriet, P. Carrez, P. Cordier, Ultimate Mechanical Properties of Forsterite, Minerals 9 (2019) 787, doi:10.3390/min9120787.
[12] Y.I. Golovin, Nanoindentation and mechanical properties of solids in submicrovolumes, thin near-surface layers, and films: A Review, Phys. Solid State. 50 (2008) 2205–2236, doi:10.1134/S1063783408120019.
[13] J.M. Wheeler, Mechanical phase mapping of the Taza meteorite using correlated high-speed nanoindentation and EDX, J. Mater. Res. (2020) 1–11, doi:10.1557/jmr.2020.207.
[14] K. Durst, V. Maier, Dynamic nanoindentation testing for studying thermally activated processes from single to nanocrystalline metals, Curr. Opin. Solid State Mater. Sci. 19 (2015) 340–353, doi:10.1016/j.cossms.2015.02.001.
[15] P. Baral, G. Guillonneau, G. Kermouche, J.-M. Bergheau, J.-L. Loubet, A new long-term indentation relaxation method to measure creep properties at the micro-scale with application to fused silica and PMMA, Mech. Mater. 137 (2019) 103095, doi:10.1016/j.mechmat.2019.103095.
[16] D. Tabor, The hardness of solids, Rev. Phys. Technol. 1 (1970) 145, doi:10.1088/0034-6683/1/3/I01.
[17] M.J. Mayo, R.W. Siegel, a. Narayanasamy, W.D. Nix, Mechanical properties of nanophase TiO_2 as determined by nanoindentation, J. Mater. Res. 5 (1990) 1073–1082, doi:10.1557/JMR.1990.1073.
[18] A. van der Rest, H. Idrissi, F. Henry, A. Favache, D. Schryvers, J. Proost, J.P. Raskin, Q. Van Overmeere, T. Pardoen, Mechanical behavior of ultrathin sputter deposited porous amorphous Al_2O_3 films, Acta Mater 125 (2017) 27–37, doi:10.1016/j.actamat.2016.11.037.
[19] M.R. Vanlandingham, N.K. Chang, P.L. Drzal, C.C. White, S.H. Chang, Viscoelastic characterization of polymers using instrumented indentation. I. Quasi-static testing, J. Polym. Sci. Part B Polym. Phys. 43 (2005) 1794–1811, doi:10.1002/polb.20454.
[20] Q. Zhou, J. Zhao, J.Y. Xie, F. Wang, P. Huang, T.J. Lu, K.W. Xu, Grain size dependent strain rate sensitivity in nanocrystalline body-centered cubic metal thin films, Mater. Sci. Eng. A. 608 (2014) 184–189, doi:10.1016/j.msea.2014.04.080.
[21] Y.S. Mohammed, D.S. Stone, A.A. Elmustafa, Strain Rate Sensitivity of the Nanoindentation Creep of Ag, Cu, and Ni Thin Films, JOM 71 (2019) 3734–3743, doi:10.1007/s11837-019-03634-1.
[22] B. Evans, C. Goetze, The temperature variation of hardness of olivine and its implication for polycrystalline yield stress, J. Geophys. Res. 84 (1979) 5505–5524, doi:10.1029/JB084iB10p05505.
[23] K. Kranjc, Z. Rouse, K.M. Flores, P. Skemer, Low-temperature plastic rheology of olivine determined by nanoindentation, Geophys. Res. Lett. 43 (2016) 176–184, doi:10.1002/2015GL065837.
[24] K.M. Kumamoto, C.A. Thom, D. Wallis, L.N. Hansen, D.E.J. Armstrong, J.M. Warren, D.L. Goldsby, A.J. Wilkinson, Size effects resolve discrepancies in 40 years of work on low-temperature plasticity in olivine, Sci. Adv. 3 (2017) 1–7, doi:10.1126/sciadv.1701338.
[25] C.A. Thom, E.E. Brodsky, R.W. Carpick, G.M. Pharr, W.C. Oliver, D.L. Goldsby, Nanoscale Roughness of Natural Fault Surfaces Controlled by Scale-Dependent

Yield Strength, Geophys. Res. Lett. 44 (2017) 9299–9307, doi:10.1002/2017GL074663.
[26] S. Koizumi, T. Hiraga, T.S. Suzuki, Vickers indentation tests on olivine: size effects, Phys. Chem. Miner. (2020) 47, doi:10.1007/s00269-019-01075-5.
[27] R. Dohmen, H.-W. Becker, E. Meißner, T. Etzel, S. Chakraborty, Production of silicate thin films using pulsed laser deposition (PLD) and applications to studies in mineral kinetics, Eur. J. Mineral. 14 (2002) 1155–1168, doi:10.1127/0935-1221/2002/0014-1155.
[28] C.Le Guillou, R. Dohmen, D. Rogalla, T. Müller, C. Vollmer, H.W. Becker, New experimental approach to study aqueous alteration of amorphous silicates at low reaction rates, Chem. Geol. 412 (2015) 179–192, doi:10.1016/j.chemgeo.2015.06.027.
[29] W.C. Oliver, G.M. Pharr, An improved technique for determining hardness and elastic modulus using load and displacement sensing indentation experiments, J. Mater. Res. 7 (1992) 1564–1583, doi:10.1557/JMR.1992.1564.
[30] W.C. Oliver, G.M. Pharr, Measurement of hardness and elastic modulus by instrumented indentation: Advances in understanding and refinements to methodology, J. Mater. Res. 19 (2004) 3–20, doi:10.1557/jmr.2004.19.1.3.
[31] S. Bec, A. Tonck, J.L. Loubet, A simple guide to determine elastic properties of films on substrate from nanoindentation experiments, Philos. Mag. 86 (2006) 5347–5358, doi:10.1080/14786430600660856.
[32] P. Baral, G. Guillonneau, G. Kermouche, J.-M. Bergheau, J.-L. Loubet, Theoretical and experimental analysis of indentation relaxation test, J. Mater. Res. 32 (2017) 2286–2296, doi:10.1557/jmr.2017.203.
[33] J.L. Hay, W.C. Olive, A. Bolshakov, G.M. Pharr, Using the Ratio of Loading Slope and Elastic Stiffness to Predict Pile-Up and Constraint Factor During Indentation, MRS Proc 522 (1998) 101, doi:10.1557/PROC-522-101.
[34] G. Kermouche, J.L. Loubet, J.M. Bergheau, An approximate solution to the problem of cone or wedge indentation of elastoplastic solids, Comptes Rendus - Mec 333 (2005) 389–395, doi:10.1016/j.crme.2005.04.001.
[35] G. Kermouche, J.L. Loubet, J.M. Bergheau, Extraction of stress-strain curves of elastic-viscoplastic solids using conical/pyramidal indentation testing with application to polymers, Mech. Mater. 40 (2008) 271–283, doi:10.1016/j.mechmat.2007.08.003.
[36] A.A. Elmustafa, S. Kose, D.S. Stone, The strain-rate sensitivity of the hardness in indentation creep, J. Mater. Res. 22 (2007) 926–936, doi:10.1557/jmr.2007.0107.
[37] R. Limbach, B.P. Rodrigues, L. Wondraczek, Strain-rate sensitivity of glasses, J. Non. Cryst. Solids. 404 (2014) 124–134, doi:10.1016/j.jnoncrysol.2014.08.023.
[38] G. Kermouche, J.L. Loubet, J.M. Bergheau, A new index to estimate the strain rate sensitivity of glassy polymers using conical/pyramidal indentation, Philos. Mag. 86 (2006) 5667–5677, doi:10.1080/14786430600778682.
[39] D.S. Stone, J.E. Jakes, J. Puthoff, A.A. Elmustafa, Analysis of indentation creep, J. Mater. Res. 25 (2010) 611–621, doi:10.1557/JMR.2010.0092.
[40] J. Chen, Y.N. Shi, K. Lu, Strain Rate Sensitivity of a Nanocrystalline Cu–Ni–P Alloy, J. Mater. Res. 20 (2005) 2955–2959, doi:10.1557/JMR.2005.0387.
[41] C.D. Gu, J.S. Lian, Q. Jiang, W.T. Zheng, Experimental and modelling investigations on strain rate sensitivity of an electrodeposited 20 nm grain sized Ni, J. Phys. D. Appl. Phys. 40 (2007) 7440–7446, doi:10.1088/0022-3727/40/23/027.
[42] M. Ghidelli, S. Gravier, J.-J. Blandin, P. Djemia, F. Mompiou, G. Abadias, J.-P. Raskin, T. Pardoen, Extrinsic mechanical size effects in thin ZrNi metallic glass films, Acta Mater 90 (2015) 232–241, doi:10.1016/j.actamat.2015.02.038.
[43] D. Pan, A. Inoue, T. Sakurai, M.W. Chen, Experimental characterization of shear transformation zones for plastic flow of bulk metallic glasses, Proc. Natl. Acad. Sci. 105 (2008) 14769–14772, doi:10.1073/pnas.0806051105.
[44] G. Guillonneau, G. Kermouche, S. Bec, J.-L.L. Loubet, Extraction of Mechanical Properties with Second Harmonic Detection for Dynamic Nanoindentation Testing, Exp. Mech. 52 (2012) 933–944, doi:10.1007/s11340-011-9561-5.
[45] B.N. Lucas, W.C. Oliver, G.M. Pharr, J.-L. Loubet, Time Dependent Deformation During Indentation Testing, MRS Proc 436 (1996) 233, doi:10.1557/PROC-436-233.
[46] R. Saha, W.D. Nix, Effects of the substrate on the determination of thin film mechanical properties by nanoindentation, Acta Mater 50 (2002) 23–38, doi:10.1016/S1359-6454(01)00328-7.
[47] J.D. Bass, Elasticity of Minerals, Glasses, and Melts, in: 1995: pp. 45–63. https://doi.org/10.1029/RF002p0045.
[48] P. Richet, F. Leclerc, L. Benoist, Melting of forsterite and spinel, with implications for the glass transition of Mg_2 SiO_4 liquid, Geophys. Res. Lett. 20 (1993) 1675–1678, doi:10.1029/93GL01836.
[49] M. Misawa, F. Shimojo, First-Principles Study of Pressure-Induced Amorphization of Fe_2SiO_4 Fayalite, Phys. Status Solidi Basic Res. 2000173 (2020) 1–8, doi:10.1002/pssb.202000173.
[50] A.A. Elmustafa, D.S. Stone, Strain rate sensitivity in nanoindentation creep of hard materials, J. Mater. Res. 22 (2007) 2912–2916, doi:10.1557/JMR.2007.0374.
[51] A. Argon, Inelastic behavior of non-polymeric glasses, in: Phys. Deform. Fract. Polym., Cambridge University Press, Cambridge, 2013, pp. 174–227, doi:10.1017/CBO9781139033046.009.
[52] J.D. Birle, G.V. Gibbs, P.B. Moore, J.V. Smith, Crystal Structures of Natural Olivines, Am. Mineral. 53 (1968) 807–824.
[53] H.J. Frost, M.F. Ashby, Deformation-mechanism maps: The plasticity and creep of metals and ceramics, Pergamon Press, 1982.
[54] C. Bollinger, K. Marquardt, F. Ferreira, Intragranular plasticity vs. grain boundary sliding (GBS) in forsterite: Microstructural evidence at high pressures (3.5–5.0 GPa), Am. Mineral. 104 (2019) 220–231, doi:10.2138/am-2019-6629.